VILNIUS UNIVERSITY

CENTER FOR PHYSICAL SCIENCES AND TECHNOLOGY

SIMONAS KIČAS

FABRICATION, CHARACTERIZATION AND APPLICATION OF DISPERSIVE GRADIENT REFRACTIVE INDEX MULTILAYERED SYSTEMS

Summary of doctoral thesis,

Technological sciences, Material engineering (08 T)

Vilnius, 2016

Dissertation was prepared in 2011–2015 at the Center for Physical Sciences and Technology (CPST).

Scientific supervisor:

Dr. Ramutis Drazdys (Center for Physical Sciences and Technology, Lithuania, Technological sciences, 08 T).

Consultant:

Prof. Kęstutis Staliūnas (Universitat Politècnica de Catalunya, Physical science, Physics – 02P)

Doctoral thesis will be defended at the Center for Physical Sciences and Technology in the senate of Material engineering:

Chairman:

Prof. dr. Roaldas Gadonas (Vilnius University, Technological science, Material engineering – 08T);

Members:

prof. habil. dr. Arūnas Krotkus (CPST, Technological science, Material engineering – 08T);

dr. Arūnas Varanavičius (Vilnius University, Physical science, Physics – 02P);

dr. Tomas Tamulevičius (KTU, Technological science, Material engineering – 08T);

dr. Vladimir Pervak (Ludwig-Maximilians – Universitat Munchen, Technological science, Material engineering – 08T).

This thesis will be considered under open session of Material engineering council on 12th of September, 2016 10 a.m. at the hall of CPST Institute of Physics.

Address: Savanorių ave. 231, LT-02300 Vilnius, Lithuania.

Summary of doctoral thesis was distributed on 12-th of August, 2016.

Doctoral thesis is available at libraries of CPST and Vilnius University.

VILNIAUS UNIVERSITETAS

FIZINIŲ IR TECHNOLOGIJOS MOKSLŲ CENTRAS

SIMONAS KIČAS

DAUGIASLUOKSNIŲ KINTAMO LŪŽIO RODIKLIO SISTEMŲ SU KONTROLIUOJAMA DISPERSIJA FORMAVIMAS, CHARAKTERIZAVIMAS IR TAIKYMAI

Daktaro disertacija

Technologijos mokslai, Medžiagų inžinerija (08 T)

Vilnius, 2016

Disertacija rengta 2011–2015 metais Fizinių ir technologijos mokslų centre

Mokslinis vadovas:

dr. Ramutis Drazdys (Fizinių ir technologijos mokslų centras, technologijos mokslai, medžiagų inžinerija – 08T).

Mokslinis konsultantas:

prof. habil. dr. Kęstutis Staliūnas (Katalonijos politechnikos universitetas, fiziniai mokslai, fizika – 02P).

Disertacija ginama Vilniaus universiteto Medžiagų inžinerijos mokslo krypties taryboje:

Pirmininkas – prof. dr. Roaldas Gadonas (Vilniaus universitetas, technologijos mokslai, medžiagų inžinerija – 08T).

Nariai:

prof. habil. dr. Arūnas Krotkus (Fizinių ir technologijos mokslų centras, technologijos mokslai, medžiagų inžinerija – 08T);

dr. Arūnas Varanavičius (Vilniaus universitetas, fiziniai mokslai, fizika – 02P);

dr. Tomas Tamulevičius (Kauno technologijos universitetas, technologijos mokslai, medžiagų inžinerija – 08T);

dr. Vladimir Pervak (Miuncheno Liudviko Maksimiliano universitetas, technologijos mokslai, medžiagų inžinerija – 08T).

Disertacija bus ginama viešame Medžiagų inžinerijos krypties tarybos posėdyje 2016 m. rugsėjo mėn. 12 d. 10 val. Fizinių ir technologijos mokslų centro didžiojoje auditorijoje.

Adresas: Savanorių pr. 231, Vilnius, Lietuva.

Disertacijos santrauka išsiuntinėta 2016 m. rugpjūčio mėn. 12 d.

Disertaciją galima peržiūrėti Fizinių ir technologijos mokslų centro Vilniaus universiteto bibliotekose ir VU interneto svetainėje adresu: www.vu.lt/lt/naujienos/ivykiu-kalendorius

Introduction

The first picture of a moving body was made in order to analyze the movement of objects too fast for the human eye to be clearly identified. In the famous article by J.D.B Stillman and E. Muybridge a running horse was the object. An example much closer to nowadays' realities would be pump-probe spectroscopy, which was introduced in the 19th century for exploring shock waves. So, in order to analyze short processes which change rapidly in time, we need as short as possible light pulses, as they define time the resolution of our experiments or setups. Laser sources exceeding long pulses were a breakthrough [1, 2]. Only several decades had passed until the first ultrashort pulses were demonstrated using passive-mode synchronization in dye lasers [3]. Since then, ultrashort pulse systems became a universal tool to make not only scientific research but were also used in industrial, medical and other applications. Pulses exceeding several optical cycles were used to monitor molecular dynamics, to make the micromachining of various materials [4].

One of the main characteristics of the short pulse is a broad spectral range. All these spectral components in the pulse have to be in a specific manner or, as it is called, "in phase" to form a transform limited pulse [5]. This means that the pulse is then travelling in a dispersive medium, and phase changes have to be compensated to maintain it short. Several different methods have been proposed over the years. Most of them are based on diffraction gratings [6], prism pairs [7], dispersive mirror [8–11] or a combination of these methods [5, 12]. Each of the aforementioned methods has its benefits and drawbacks. The grating and prism systems can create large amounts of negative dispersion, but they are sensible to alignment errors, have a low efficiency and cannot compensate a higher-order dispersion in a wide spectral range. Meanwhile, dispersive mirrors can efficiently compensate a higher-order dispersion, are easy to align, but can create a limited amount of dispersion [13]. However, today dispersive mirrors are most widely used when it comes to pulse compression, mostly because of the alignment advantage and flexibility to have a varying dispersion in a wide spectral range [14–16]. Since the first demonstration of a chirped mirror in 1994 [9], a lot of different designs have been proposed to modify the classical one. At present, it is possible to distinguish at least five most popular types of

these mirrors: double-chirped [17–19], Brewster [20, 21], complementary pair [16, 22, 23], high dispersion (HDM) [11, 14, 24], BASIC [25] mirrors. Each type has its own benefits, but in general they all are trying to solve several problems related to chirped mirrors: 1) GVD dispersion oscillations caused by interference at the interface between the air and the mirror surface; 2) a large GVD characteristic sensitivity to deposition errors; 3) the amount of GVD introduced in one bounce from such a mirror.

Along with the above mentioned tasks, chirped mirrors have to withstand the requirements of the ever-growing need for a higher power of ultrashort systems. Recently created laser oscillators and amplifiers based on the fiber [26, 27] or the thin-disk technology [27] can generate sub-picosecond pulses with the energy of up to tens of μJ and the repetition rate close to 10 MHz, thus reaching hundreds of watts as an average power or several gigawatts as the peak power. The laser-induced damage mechanisms at these power levels are unavoidable. One of the weakest elements in respect of LIDT in ultrafast systems is optical coatings. The resistance of optical elements to laser exposure was one of the main topics after the first laser pulses had been demonstrated. Laser damage studies in the nanosecond regime were published in variety of papers and are still an interesting topic for both science and industry. After femtosecond pulses had been demonstrated, optical resistance in this field became an interesting issue, too. However, most of studies in this field are carried out at the so called 1-on-1 regime, or using pulse trails at a kHz repetition rate. It should be noted that the laser resistance of dispersive coatings is a rather new field, and only several papers on this topic have been published recently.

Objective of the thesis

To enhance the characteristics and to extend the application area of negative dispersion multilayer coatings by optimizing the ion beam sputtering technologies for sputtered mixed materials and optimizing their coating design.

The scientific tasks of this work

- To create a method for controlling residual stress in ion beam sputtered multilayer coatings based on a mixture of co-deposition and post-deposition annealing procedure combinations.

- To apply the method for residual stress control to high reflection multilayer coatings sputtered by the ion beam technology on thin substrates, meeting the high requirements for surface flatness.

- To design and implement the BASIC mirror with an ultra-broadband negative dispersion range, using the residual stress control method based on the Nb_2O_5–SiO_2 co-sputtering and annealing technology combination.

- To determine and optimize the laser-induced damage threshold for negative dispersion coatings in the ultrafast regime, using electric field reallocation in the coating structure.

- To apply the design and manufacturing principles of negative dispersion coatings to construct and implement a mirror capable of focusing a single wavelength light beam in the reflection mode.

- To optimize the focusing characteristics in a linearly tailored layer structure by incorporating the Gires–Tournois interferometer structure and multiple optimized GTI structures to enhance the focal distance characteristics.

Scientific novelty

Dispersive multilayer coatings today are inseparable from ultrashort systems and lasers. In this work, attention is focused on optimizing the existing characteristics or finding the new applications or designs for this specific kind of optical coatings.

In this work, to our knowledge for the first time, a new method to control and compensate residual stress in ion beam sputtered coatings is demonstrated. The method combines two well-known technologies: material mixing by co-deposition and *ex-situ* annealing, which enables us to reach the surface flatness values equal to those of an uncoated surface, or even better, for a sufficiently thick multilayer high reflectors or ultra-

broadband negative dispersion mirrors (BASIC design). The implementation of stress control for the BASIC mirror results in creating a large amount of negative GDD versus the wavelength band close to theoretical predictions.

As the introduced amount of GDD per one bounce from a mirror is increased, electric field strength can become extremely large, and thus the LIDT values of an element can be drastically reduced. In this work, the femtosecond pulse LIDT for negative dispersion coatings and the dependence on electric field strength enhancement inside a multilayer structure are examined in detail. A method of reducing and reallocating the inner electric field distribution, based on the measured LIDT values of thin monolayers of pure and mixed materials, is proposed to increase the LIDT values up to several times.

Finally, for the first time, the focusing effect based on negative dispersion in the reflection from a flat multilayer dielectric mirror is demonstrated. The focal distance of several hundreds of microns is reached with an optimized design based on multiple GTI structures with a non-uniform layer distribution.

Statements to defend

1. Co-deposition of high refractive index materials such as Nb_2O_5, Ta_2O_5 with the low index material SiO_2 in combination with the *ex-situ* post-deposition annealing enables to make multilayer structures with a completely compensated residual stress after the annealing cycle with optimized temperature and time parameters.

2. The elimination of residual stress in a multilayer coating enables to design and implement the BASIC mirror construction on a thin (<0.35 mm thickness) substrate, thus allowing to reach a broad highly negative dispersion (spectral width 200 nm with a central wavelength and $GDD = -200\,fs^2$) range with the initial surface flatness of the element.

3. Laser-induced damage threshold values in the ultrafast regime strongly depend on the high refractive index materials being used and on their band gap values in particular. The electric field distribution optimization with respect to high or low

band gap material layers and layer interfaces enables to increase the LIDT up to 2.5 times without any notable decrease in other specifications.

4. Different angular components having different penetrations depths in multilayer coating structure can result in negative diffraction and thus focusing in reflection from a high reflection mirror structure with optimized layer thicknesses in the same manner as in chirped dielectric negative dispersion mirrors.

Approbation

ISI scientific papers directly related to the thesis:

I. **S. Kičas**, U. Gimževskis, S. Melnikas, Post deposition annealing of IBS mixture coatings for compensation of film induced stress, Opt. Mat. Express*, **6**(7), 2236-2243 (2016).

II. Y. C. Cheng, **S. Kičas**, and K. Staliūnas, Flat focusing in reflection from a chirped dielectric mirror with a defect layer, NANOP, **9**(1), 093084-093084 (2015).

III. Y. C. Cheng, **S. Kičas**, J. Trull, M. Peckus, C. Cojocaru, R. Vilaseca*, et al.*, Flat Focusing Mirror, Scientific Reports*, **4** 6326 (2014).

IV. Y. C. Cheng, M. Peckus, **S. Kičas**, J. Trull, C. Cojocaru, R. Vilaseca*, et al.*, Beam focusing in reflection from flat chirped mirrors, Physical Review A*, **87**(4), 045802 (2013).

V. X. Fu, A. Melnikaitis, L. Gallais, **S. Kičas**, R. Drazdys, V. Sirutkaitis*, et al.*, Investigation of the distribution of laser damage precursors at 1064 nm, 12 ns on Niobia-Silica and Zirconia-Silica mixtures, Opt. Express*, **20**(23), 26089-26098 (2012).

VI. B. Mangote, L. Gallais, M. Commandre, M. Mende, L. Jensen, H. Ehlers, M. Jupe, D. Ristau, A. Melninkaitis, J. Mirauskas, V. Sirutkaitis, **S. Kičas**, T. Tolenis, and R. Drazdys, Femtosecond laser damage resistance of oxide and mixture oxide optical coatings, Opt. Lett.*, **37**(9), 1478-1480 (2012).

VII. Melninkaitis, T. Tolenis, L. Mažulė, J. Mirauskas, V. Sirutkaitis, B. Mangote, X. Fu, M. Zerrad, L. Gallais, M. Commandrs, **S. Kičas**, R. Drazdys, Characterization of zirconia- and niobia- silica mixture coatings produced by ion-beam sputtering, Appl. Opt.*,* **50**(9), C188-C196 (2011).

Other scientific papers directly related to the thesis:

1. **S. Kičas**, G. Batavičiūtė, K. Juškevičius, T. Tolenis, R. Drazdys, R. Buzelis, and A. Melninkaitis, Characterization and application of $HfO_2 – SiO_2$ mixtures produced by ion-beam sputtering technology, Proc. SPIE **8885**, 888521 (2013).

2. Y. C. Cheng, M. Peckus, **S. Kičas**, J. Trull, C. Cojocaru, Diffraction control of reflected beam by chirped mirror, Proc. SPIE **8771**, 87710W (2013).

3. K. Stankevičiūtė, S. Melnikas, **S. Kičas**, V. Sirutkaitis, L. Trisauskas, M. Vengris, J. Vengelis, R. Grigonis, Synchronously pumped femtosecond optical parametric oscillator with broadband chirped mirrors, Proc. SPIE **9503**, 950312 (2015).

4. Fu, XH, A. Melninkaitis, L. Gallais, **S. Kičas,** R. Drazdys, V. Sirutkaitis, M. Commandre, Measured nosecond laser damage probabilities of Niobia- Silica and Zirconia-Silica mixtures coatings, Proc. SPIE **8530**, 85300X (2012).

5. L. Gallais, B. Mangote, M. Commandre, M. Mende, L. Jensen, H. Ehlers, M. Jupe, D. Ristau, A. Melninkaitis, V. Sirutkaitis, **S. Kičas,** T. Tolenis, R. Drazdys, An exhaustive study of laser damage in ion beam sputtered pure and mixture oxide thin films at 1030nm with 500fs pulse durations, Proc. SPIE **8530**, 85300K (2012).

6. Melninkaitis, T. Tolenis, L. Mažulė, J. Mirauskas, V. Sirutkaitis, B. Mangote, X. Fu, M. Zerrad, L. Gallais, M. Commandrs, **S. Kičas**, R. Drazdys, Complex study of zirconia-silica and niobia-silica composite coatings produced by ion beam sputtering, Proc. SPIE **7842**, 784203 (2010).

7. X. Fu, A. Melninkaitis, L. Gallais, **S. Kičas**, R. Drazdys, V. Sirutkaitis*, et al.*, Measured nanosecond laser damage probabilities of niobia-silica and zirconia-silica mixtures coatings, Proc. SPIE **8530**, 85300X (2012).

Summary of doctoral thesis

Doctoral thesis contains 5 chapters.

Chapter 1. Literature survey

In this chapter, the basics of ultrashort pulse generation and dispersive pulse broadening in normal dispersion media are reviewed. Principle of chirped mirror operation and existing types of dispersive coatings are discussed. The main advantages and drawbacks are indicated as well as limitations and main issues related to these specific elements are concluded. Calculation of thin film stack spectral performance by well-known matrix method is reviewed and optimization algorithms are discussed. Finally, main PVD methods for thin films deposition and resulting layer microstructure is described.

Chapter 2. Residual stress in sputtered multilayer coatings

In this chapter influence of using ion beam sputtered mixtures instead of pure materials and impact of applied post deposition annealing to residual stress is investigated. Single layer pure films and mixtures of Nb_2O_5 / SiO_2 as well as multilayer coatings are examined by the means of residual stress. Pure and mixed monolayer samples were annealed at various temperatures and residual stress was determined after each annealing routine. Residual changes in optical constants, layer thickness and surface roughness upon annealing are examined to explain stress behavior.

8 different in volumetric fraction single layer coatings of Nb_2O_5 / SiO_2 were produced. Common features of mixed oxide coatings like blue shift of absorption edge in UV range [28] and scaling of refractive indices according to volumetric fraction [29], are evident and depicted in Fig. 1.
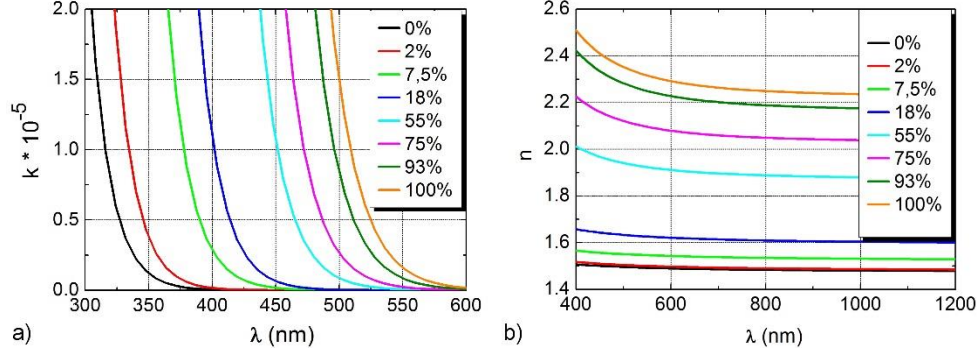
Fig. 1. Extinction coefficient (a) and refractive index dispersion (b) of Nb_2O_5 and SiO_2 mixtures according to volumetric fraction of Nb_2O_5.

An increase in physical thickness by 1.1–1.4% was observed for all single layer samples after annealing to 300 C°. Meanwhile, a decrease in average refractive index by 0.4–0.6% was also determined from transmittance spectra. Resulting increase of approximately 1 % in optical thickness is in good agreement with other published papers and can be explained with a void formation under high temperature annealing of IBS coatings [30, 31]. Void formation was also confirmed by a slight increase in surface roughness according to AFM measurements. Profilometric measurements of substrate's surface bending were performed on fused silica samples of 1 mm thickness, designated for stress determination. Residual film stress was calculated using Stoney equation:

$$\sigma = \frac{1}{6}\left(\frac{1}{R_2} - \frac{1}{R_1}\right)\frac{E}{1-\nu}\frac{t_s^2}{t_f},\tag{1}$$

where t_s is substrate's and t_f is film's thickness respectively, R_2, R_1 – radius of curvature before and after deposition respectively, $E = 72\times10^3$ N/mm^2 and $\nu = 0.17$ – Young's modulus and Poisson coefficient of the fused silica substrate respectively [32]. Calculated residual stress for Nb_2O_5 / SiO_2 mixtures before and after each annealing step is depicted in Fig. 2 a. For mixed materials resulting stress can be made even smaller than for pure ones after annealing. This result was also observed in before mentioned publications [29, 33] and is related to microstructural differences between pure and mixed materials. Several stress components can be distinguished as a drop in compressive stress for SiO_2 and Nb_2O_5 is slightly different. While thermal expansion coefficients of FS (0.55×10^{-6}/C°) and SiO_2 should be similar a drop in stress after annealing can be related to relaxation of compressed

structure which is in agreement with increased thickness. In the case of Nb_2O_5 which has larger CTE ($5.8 \times 10^{-6}/C°$) a slightly larger reduction of stress is observed. This difference in stress behavior can be assigned to the thermal stress induced by a different CTE of substrate and coating. It is also well known that incorporation of small fraction of other material prevents thin oxide film structure from crystallization effect [29] which was not observed at any of samples mentioned in the paper (Fig. 2 b).
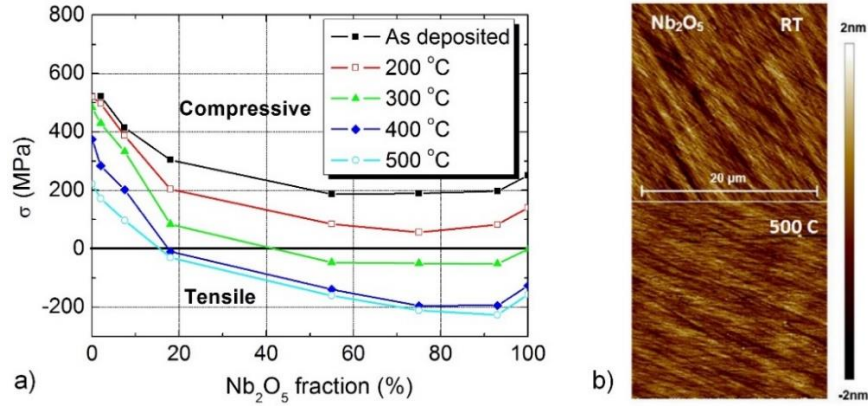
Fig. 2. Residual stress according to Nb_2O_5 fraction in monolayer mixture at different annealing temperatures. AFM measurements of pure Nb_2O_5 before and after annealing to 500 °C (b).

A modeling of resulting stress in multilayer coatings was made based on results in Fig. 4.a. An assumption was made that stress in multilayer is an average of stresses in single layers of the stack and is calculated by formula [34]:

$$\sigma_M = \frac{\sigma_H t_H + \sigma_L t_L}{t_H + t_L},$$
(2)

where σ_M is total stress in multilayer coating, $\sigma_{H,L}$ is stress and $t_{H,L}$ is total thickness of high (H) and low (L) refractive index materials in mirror. Several possible mixture's combinations were selected to make highly reflecting mirror with a theoretical reflectivity R larger than 99.9% for 1064 nm wavelength at normal angle of incidence. The coating design with 93% and 8% of Nb_2O_5 has been chosen as optimal, so that residual stress would become zero or negligible after annealing to 430°C. Theoretical prediction, using data from Fig. 2, of resulting stress for multilayer coating with a design structure $(HL)^{14}L$ using pure materials and optimized mixtures according to annealing temperature for fused silica substrates is plotted in Fig. 3.
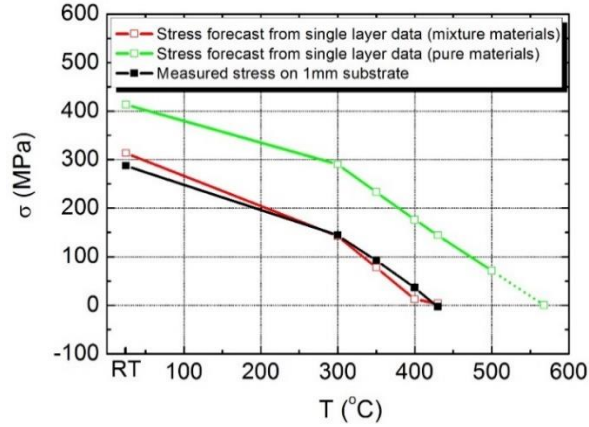
Fig. 3. Impact of annealing temperature to residual stress of mirror with optimized mixed materials.

Surface flatness interferometric measurements of aforementioned samples are depicted in Fig. 4. Measurements before and after annealing at 430 °C are only analyzed. Multilayer coatings on FS samples before temperature treatment exhibit high compressive stress resulting in measured PV values close to approximately 3λ and 10λ for 2 mm and 1 mm thickness samples respectively. However, after annealing at 430 °C, compressive stress in SiO_2 dominated low index layers is overcompensated by tensile stress in Nb_2O_5 dominated high index layers, and thus resulting in PV values lower than λ/10 for 2 mm substrate (Fig. 4) and equal to uncoated surface irregularities for 1 mm thick substrate.
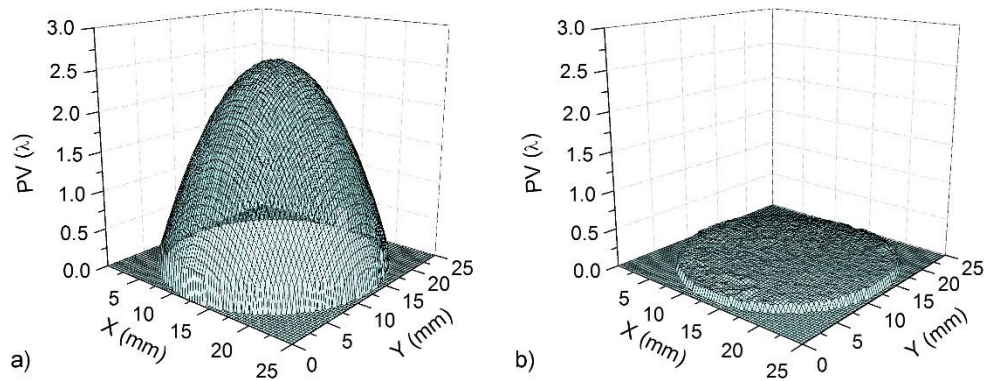
Fig. 4. Surface mapping of as deposited mirror (a) and after post deposition annealing (b) on 2 mm fused silica sample.

Chapter 3. Stress reduction in BASIC mirrors using mixtures and annealing

Back-side coated (BASIC) chirped mirror is characterized by very smooth group delay dispersion (GDD) curve over extremely wide spectral bandwidth, however these optical elements suffer from poor flatness since they combine as thin as possible substrate and highly stressed sputtered coatings. In this chapter we use ion beam sputtering technology to produce BASIC chirped mirror based on Nb_2O_5–SiO_2 mixtures and post-deposition annealing to compensate coating stress and fabricate optical element with sufficient flatness. The chirped mirror with close to the maximum achievable GDD, considering coating thickness, for given wavelength range is successfully demonstrated.

A simple chirped mirror structure with a linearly increasing Bragg wavelength with respect to layer number was chosen as a starting design for the further optimization. Several outer layers were modified manually to make GDD oscillations proper for the further computer optimization. Fused silica was used as the incident medium. Target requirements for the final design were a better than 99% average reflectivity and the maximum achievable GDD for the 250 nm wavelength range centered at 800 nm at the normal angle of incidence. The gradual evolution algorithm [35] was used to reach the desired optical properties. The resulting optimized coating layer structure consisting of Nb_2O_5 as a highly refractive index material (H) and 7.5 % volumetric fraction of Nb_2O_5 in the Nb_2O_5 / SiO_2 mixture as a low-index material is depicted in Fig. 5.

Table 1. Cauchy formula coefficients for the substrate and layer materials

	A	B	C
Fused silica	1.4465	0.0029	0.0001
Nb_2O_5	2.1985	0.0325	0.002553
Nb_2O_5 / SiO_2 mixture	1.5081	0.0056	0.0000026

The final coating design consists of 63 layers and the total thickness of 8.2 µm. Fig. 6 depicts the theoretical transmittance spectra and measurement data of the fabricated mirror. A small discrepancy between the predicted and the measured transmittance is absent, proving the presence of deposition errors. These errors may arise from layer random

or the systematic thicknesses errors or zone target position calibration error, leading to a change in the mixture volumetric fraction. The theoretical and the measured GDD curves are depicted in Fig. 6. The measured GDD curve was obtained by eliminating the positive GDD (accumulated during the double pass through the substrate) from the recorded GDD of the BASIC mirror. This subtraction allows us to properly estimate the fabrication errors. The error bars in Fig. 6 show simulated errors when 0.3% layer physical thicknesses and 0.5% refractive indices errors are statistically included with the probability corridor equal to 68%. The depicted bars here represent an area limited by the worst-case scenario where the measured GDD curve may be influenced by the mentioned errors. The recorded GDD curve fits inbetween the above-mentioned error region and exhibit the ± 100 fs^2 dispersion ripple around the average value of -300 fs^2 in the 700–880nm wavelength bandwidth. The deposition errors in the process with broadband optical monitoring tend to experience the so-called error accumulation process [36]. In combination with the typical layer sensitivity distribution in conventional CM where most sensitive layers are the ones closest to the air interface, this leads to large (larger than expected from linear error simulations) deviations in the GDD. It can be concluded that the BASIC type CM has a lower sensitivity to the error accumulation effect, because essential layers are deposited in the first place while the rest of the structure does not play an important role in the GDD characteristics.
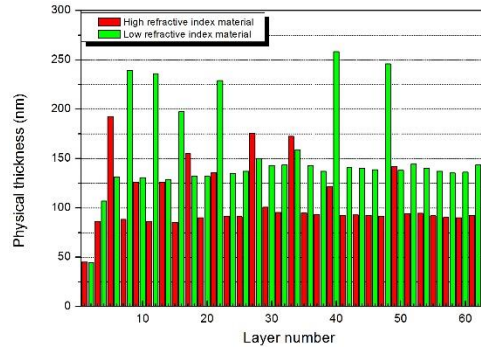

Fig. 5. Layer thicknesses of the 63-layer chirped mirror. High and low refractive index materials correspond to the Nb_2O_5 and the 7.5% Nb_2O_5/SiO_2 mixture, respectively.
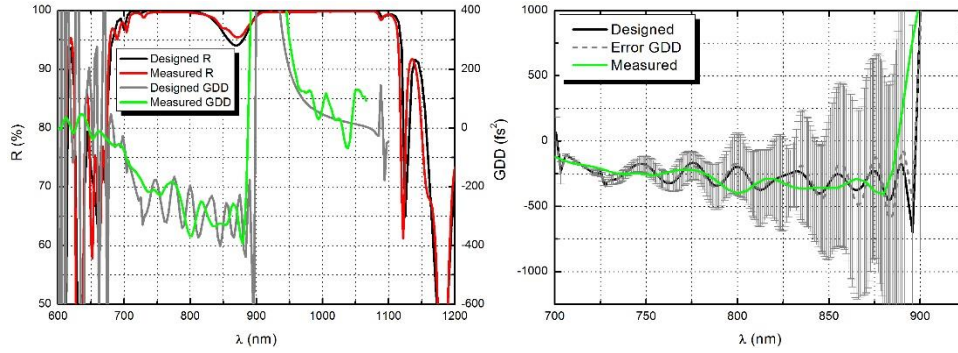
Fig. 6. Theoretical and measured reflection and GDD spectra of the BASIC mirror (left). Comparison of the predicted and the actual GDD errors (right). Vertical lines indicate the error region when 0.3% optical thicknesses errors are introduced.

The annealing process was used to reduce the residual film stress and to improve the flatness of the optical component. Fig. 7 depicts the residual element stress after annealing at different temperatures. As one can expect, the residual stress decreases with increasing the annealing temperature and becomes close to zero after annealing at 440 ℃. The change in the resulting stress is due to the increased tensile stress in the H material and the decreased compressive stress in the L material.
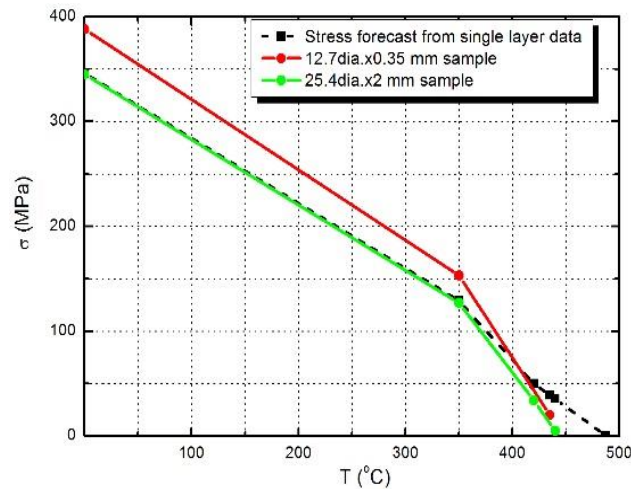

Fig. 7. Change of the residual stress with increasing the annealing temperature.

Surface flatness interferometric measurement for a 0.35 mm thickness sample after annealing is depicted in Fig. 8. After deposition, the surface flatness was close to approximately 50 λ. After annealing, the interferometric measurement showed the residual element flatness of 0.5 λ, which is close to the initial flatness of the substrate. Fig. 9 a and

17

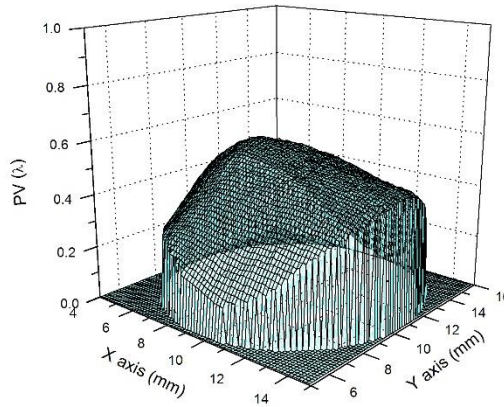b depict a comparison of transmittance and GDD spectra before and after annealing at 440 ℃.

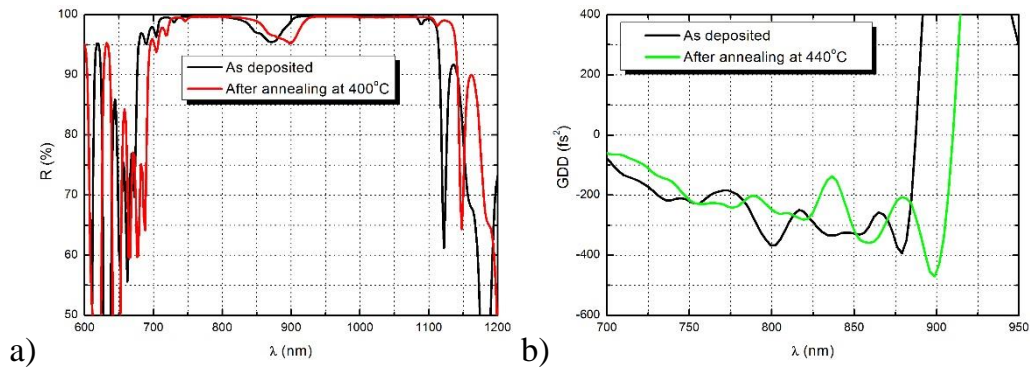Fig. 8. Surface flatness of the 0.35 mm element after the annealing procedure.

a)   b)

Fig. 9. A comparison of transmittance (a) and GDD (b) spectra before and after annealing at 440 ℃.

In both graphs, a shift of the center wavelength (CWL) can be clearly indicated. A consistent study of these effects in ion beam sputtered coatings was done, and a simple model for predicting the CWL shift during annealing was proposed by Brown [30]. The alteration of the GDD curve after annealing can be attributed to significant errors of interferometric GDD measurements.

Using the mixture materials and the annealing procedure, we were able to produce a 0.5 λ surface flatness BASIC structure chirped mirror with the close to average -200 fs2 GDD value and >99% reflectance over the 200 nm range.

Chapter 4. Optimization of laser-induced damage threshold in chirped mirrors by electric field reallocation

Dispersive multilayer dielectric coatings have been developed for the past two decades since their invention in 1995 [9]. A range of applications for various pulse compression tasks has been demonstrated [15, 37]. Different designs of dispersive mirrors, such as double-chirped mirrors [17, 38], back-side-coated chirped mirrors [25], complementary chirped mirror pairs [15], high dispersion Gires–Tournois interferometer (GTI) type mirrors [10, 11] and others [39] were created to meet the highly demanding requirements for the group delay dispersion versus bandwidth performance. The progress in the chirped mirror design and manufacturing allowed dispersion compensation up to -10000 fs^2 [40] or up to 1.5 octave bandwidth [15]. Such a bandwidth permits pulse compression up to a single cycle of the electric field oscillation [15]. However, as the optical power in common femtosecond laser applications is also increasing, damage resistance to laser radiation is one of the main remaining issues to overcome. In this chapter, the relation between the laser-induced damage threshold (LIDT) and the electric field intensity (EFI) distribution inside a CM is investigated experimentally.

The GTI-like interferometric structures with the electric field variation according to the incident angle (AOI) were designed using Ta_2O_5 and SiO_2 materials and consisted of the quarter width optical thickness (QWOT) or double QWOT layers at the wavelength of 1030 nm. Coating samples were deposited with the CEC IBS@lab ion beam sputtering (IBS) coating system with a zone target configuration. The optical broadband monitoring system with the spectral range of 400–1600 nm was used as a high-accuracy tool to control layer thickness. The variation of AOI enabled us to change and accurately control the electric field strength inside a multilayer structure [41] while neglecting the influence of small manufacturing errors: as they change only the absolute values and keep the tendency of |E^2| versus AOI the same. The resulting electric field distribution for both designs is shown in Fig. 10. In this particular case, the changing AOI enables us to analyze the LIDT behavior in accordance with the electric field. Meanwhile, inside the GTI-2 structure the

electric field distribution changes as the maximum at the Ta_2O_5/SiO_2 layer interfaces shifts to SiO_2 when the AOI changes from 0 to 40 degrees. This electric field behavior enables us to study the LIDT at the interfaces of high and low refractive index materials and to compare the LIDT values while relocating the maxima of the electric field from the interface to SiO_2 as keeping the same sample. For both aforementioned structures, the reflection curve shifts to the shorter wavelength as the AOI is increased but maintains almost the same values of reflection in the range of interest – from 1010 to 1050 nm.
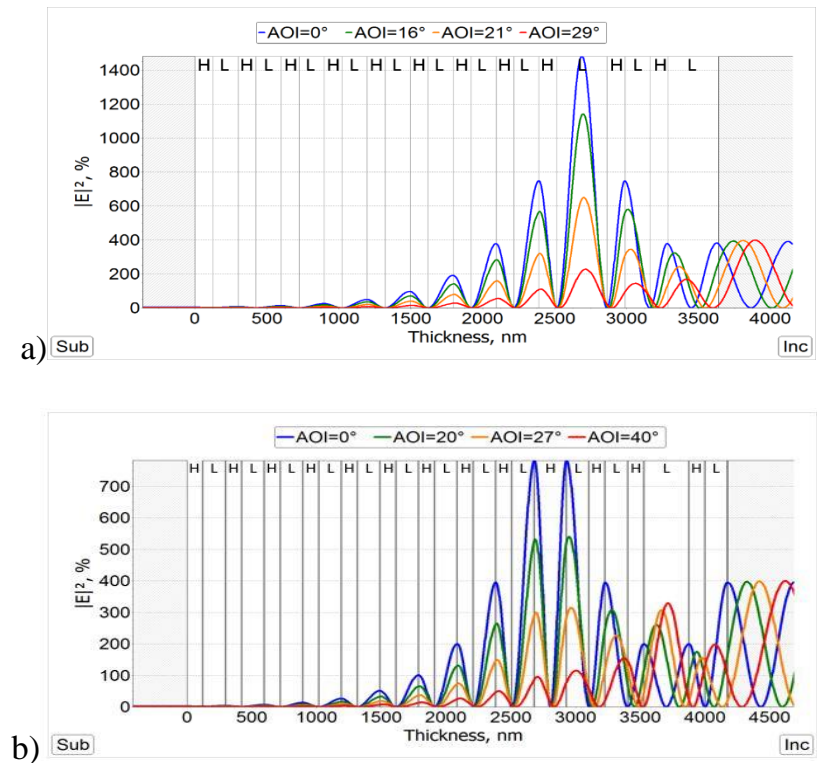

Fig. 10. Squared electric field distribution of GTI-1 (a) and GTI-2 (b) coatings.

The measured LIDTs for GTI-1 and GTI-2 are depicted in Fig. 11. For the GTI-1 structure, the LIDT values range from approximately 0.1 J/cm^2 to 0.36 J/cm^2 as the electric field strength is reduced by a factor of 7. For GTI-2 at 40°AOI, the distribution of the electric field is changed so that its maximum is positioned in the SiO_2 layer. This fact does not change the LIDT and electric field interdependence as depicted in Fig. 11b, which is still governed by the electric field strength in the high index layer.
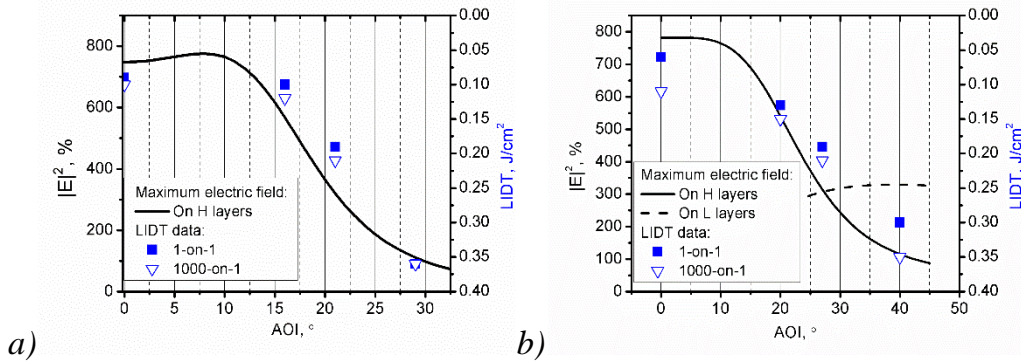
Fig. 11. LIDT and electric field dependence on measurement angle (AOI) for GTI-1 (a) and GTI-2 (b) coatings.

Several damaged sites of GTI-1 and GTI-2 coatings were inspected in detail with an optical microscope, a contact profilometer, and a SEM microscope. Both the contact profilometer and the optical microscope analyses have shown that the damage morphology is of a blister form. This fact indicates that the damage was initiated inside the coating structure. Three measured cross-sections are displayed in Fig. 12 (b, d, f). It is possible in this way to indicate the exact layers and interfaces in which the damage occurred. For all cases, only the highly refractive index material Ta_2O_5 layers or interfaces with the highest electric field strength were damaged. In the case of GTI-1 at the AOI = $0°$ damage site (Fig. 12a), even approximately double electric field strength in the SiO_2 layer did not inflict a bulk damage or any visible modification, while the nearby Ta_2O_5 layers were damaged. Based on the obtained results and observations, a strategy for a chirped mirror electric field optimization was formed: the electric field target was added in the last optimization step, considering the electric field strength in the Ta_2O_5 layers and interfaces. Meanwhile, electric field strength in SiO_2 layers was allowed to grow without any limitations.
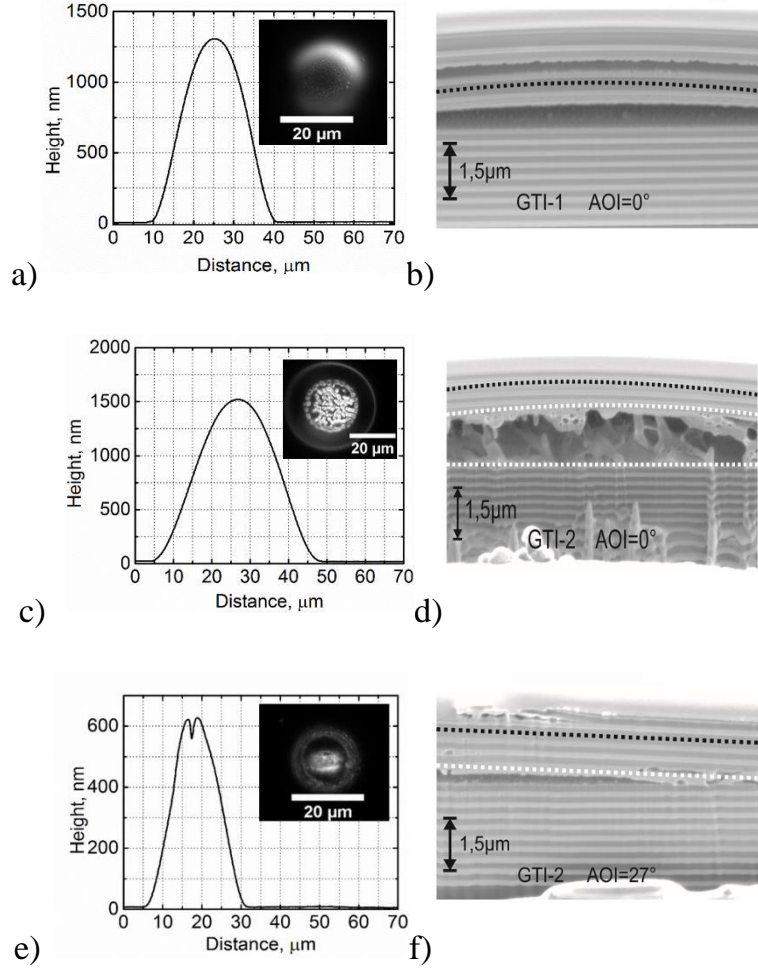
Fig. 12. Damage morphology (a, c, e inserts) and transversal surface scan measurements by a contact profilometer (a, c, d). SEM cross-section of the damaged sites (b, d, f): a, b – GTI-1 sample AOI = 0°; c, d – GTI-2 sample AOI = 0°; e, f – GTI-2 sample AOI = 27°. Dotted lines indicate resonant layers: white – H material, black – L material.

By considering the results and observations mentioned above, two additional chirped mirrors featuring different electric field distribution were designed. The first one was without electric field optimization (CM-1) and the second one – with electric field optimization (CM-2). The resulting coating designs are depicted in Fig. 13 a, b. CM-2 is specific for the optimized design, because a tendency to increase thickness for the lower refractive index layers is observed. However, the both designs result in GDD = -600 ± 100 fs^2 in the range from 1025 to 1055 nm and the reflectivity larger than 99.5% (Fig. 13 c, d), though some minor difference in the GDD oscillations and the position of reflection spectra exists.
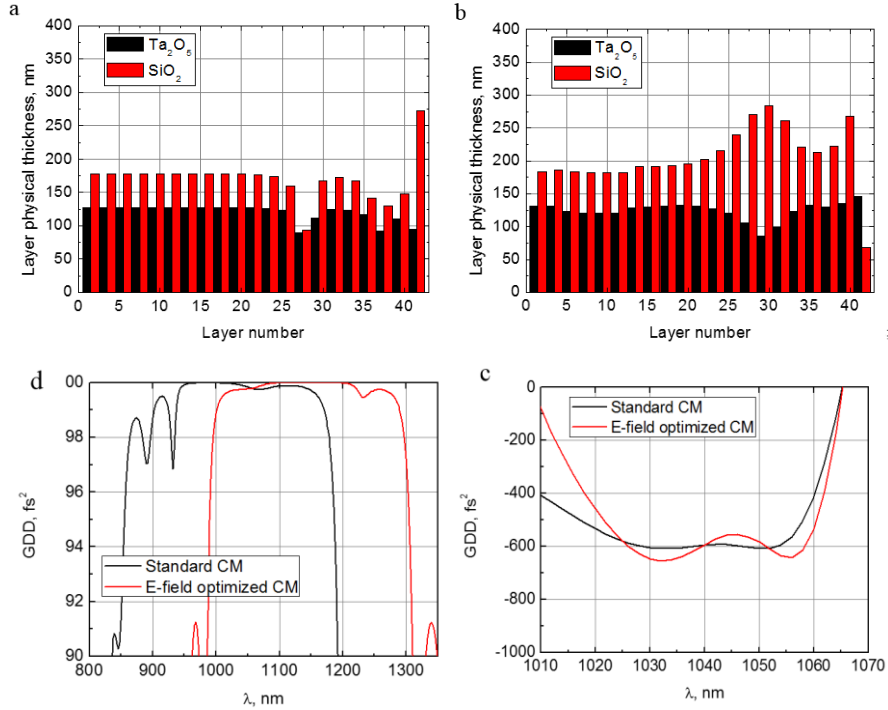
Fig. 13. Layer structure (a, b) and spectral parameters (c, d) of standard (a) and optimized electric field (b) chirped mirrors.

While spectral performance and phase characteristics are similar, electric field distribution is considerably different as depicted in Fig. 14**Error! Reference source not found.** For a standard chirped mirror, the electric field maxima are distributed almost only on the high refractive index material layers and interfaces among the layers. Meanwhile, for CM-2 chirped mirror electric field peaks are shifted to the SiO_2 layers while maintaining the electric field amplitude on the H layers as low as possible. For the CM-2 design, the maximum electric field intensity is almost two times larger on the SiO_2 layers than on interfaces among different layers.
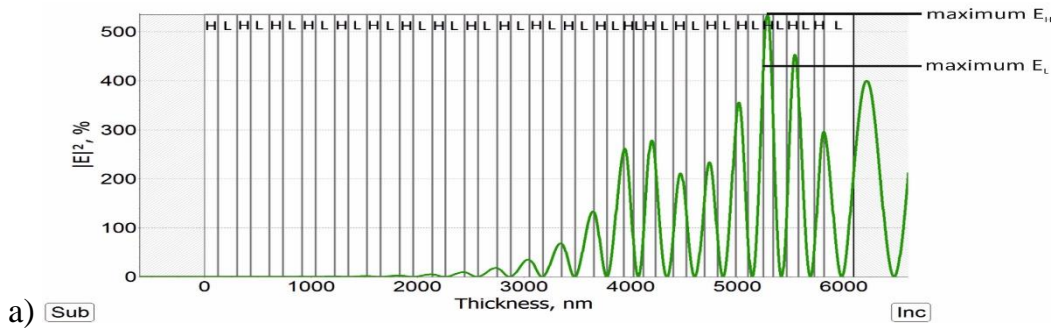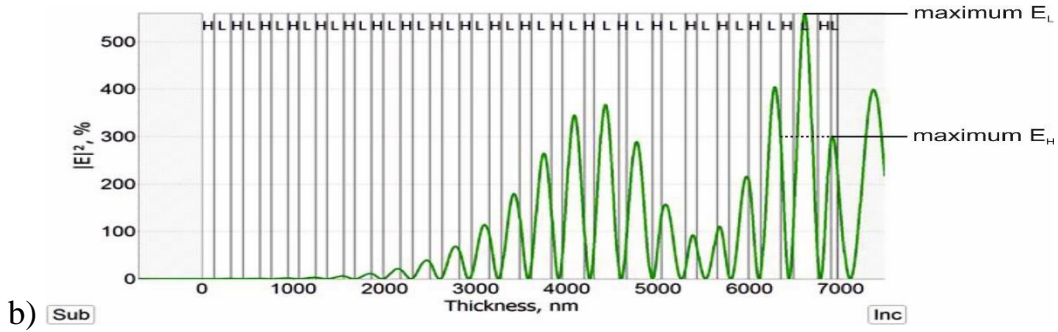
Fig. 14. Squared electric field distribution for CM-1 (a) and CM-2 (b) mirrors.

As expected, the measured LIDT for the electric-field-optimized CM-2 (0.26 ± 0.05 J/cm^2) was approximately two times larger than for standard CM-1 (0.12 ± 0.05 J/cm^2). The increase in LIDT was expected as the electric field intensity was reduced on Ta$_2$O$_5$ layers and interfaces for the CM-2 design as compared to the CM-1 design. The morphological analysis with a profilometer and an optical microscope indicates that the damage location is again inside the coating structure for both designs – no craters while observing the damage sites were noticed (Fig. 15 a, c). The SEM cross-sections analysis indicates damaged layers in coatings (Fig. 15 b, d). Selected spots were damaged at a fluence approximately by 20% higher than the LIDT values for both mirrors. In case of the CM-1 coating, a damaged layer coincides with the layer of the largest electric field intensity (Fig. 15 b). In the CM-2 mirror (Fig. 15 d), two layers were heavily damaged, and both of them slightly deviated from the maximum electric field intensity. In the first damaged layer (6th layer from the air side), the electric field intensity reached 200 %. In the second damaged layer (10th layer from the air side), the electric field intensity was below 100% and was several times smaller than in the nearby layers. The reasons for the damage of this layer are unclear and cannot be explained by the LIDT dependence on the electric field calculated using the plane wave model.
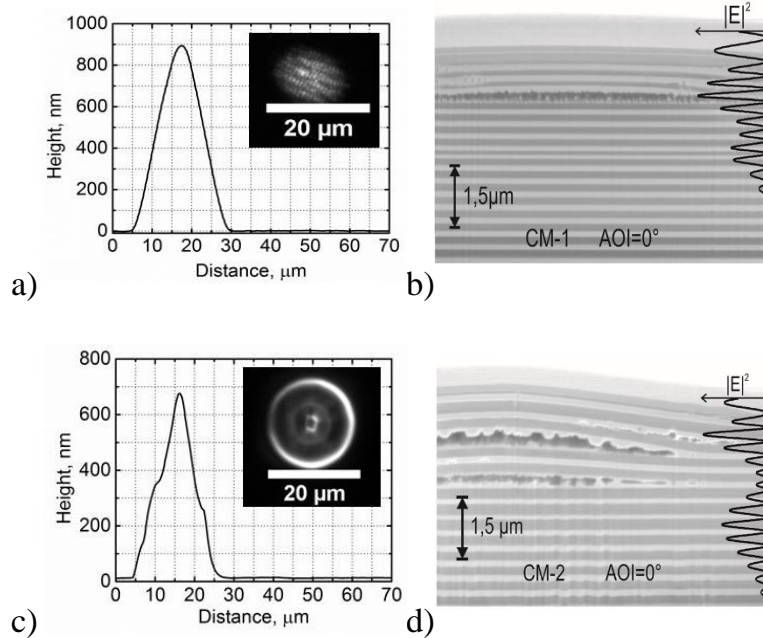
Fig. 15. Damage morphology (a, c, inserts) and transversal surface scan measurements by a contact profilometer (a, c). The SEM cross-section of damaged sites (b, d): a, b – CM-1 sample AOI = 0°; c, d – CM-2 sample AOI = 0°.

In several previous publications [42], it has been shown that the LIDT for ultrashort pulses scales linearly according to a material band gap to a certain extent [43] where the electric field intensity (EFI) should be taken into account. In Fig. 16, a summary of the obtained results is presented. A clear interdependence between the electric field amplitude on the H layer and the LIDT values for both GTI and chirped mirrors can be noticed. A saturation in LIDT, limited by a combination of EFI and the material "internal" damage threshold, can be expected at some point [44].
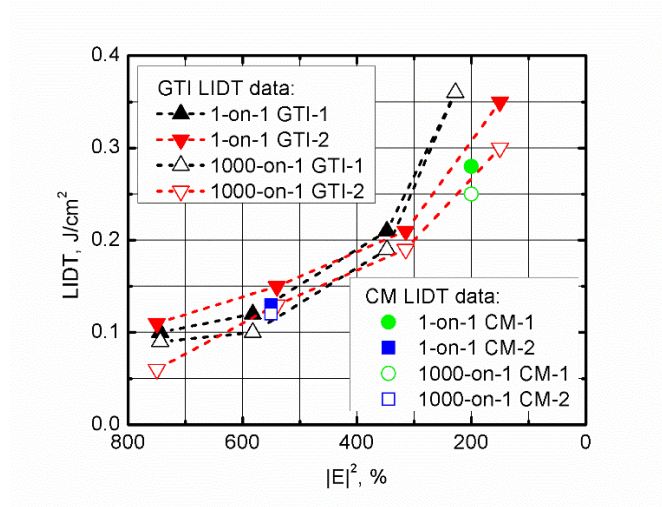
Fig. 16. LIDT dependence on maximum squared electric field in damaged layers (H layers).

Chapter 5. Focusing in reflection from flat chirped mirror

Focusing with linearly modulated chirped mirror

Spatially micro-modulated materials such as Photonic Crystals (PhCs) are known to be able to substantially modify the flow of light in both frequency, and spatial domain [45, 46]. Particularly, spatial dispersion (diffraction) of beams can be suppressed or even made negative, leading to flat lens focusing and imaging in transmission through PhCs [47]. A flat PhCs lens, consisting of a very thin slice of PhCs, can focus a beam or form light pattern image, even with a sub-wavelength resolution [48, 49]. Furthermore, optical meta-materials designed for negative refraction [50] have been proposed for flat lensing with usual and sub-wavelength resolution. The translational invariance of flat lenses in transverse direction make them principally different from the standard curved-surface or diffractive lenses, as the latter ones always possess an optical axis and thus require a precise steering and lateral positioning of the incident beam. In this chapter we show the effects of beam focusing and light-pattern imaging, with transverse invariance, by means of a flat photonic structure working in reflection instead of transmission. The principle of flat lensing in transmission relies on negative spatial dispersion of wave propagating in the material, meaning that the plane wave components at larger angles get larger phase-delays propagating through the material. For normal dispersion, in vacuum, the angular dependence of phase-delay is opposite. The concept of flat focusing mirror in reflection also should rely on the negative spatial dispersion: the interface should change the relative phases of the plane-wave components so that waves at larger incidence angle would get larger phase-delay in reflection. This effect is impossible in reflection from usual metallic or dielectric mirror, where the wave reflects directly from the interface. The dispersion, however, could be in principle manipulated if the reflecting wave would penetrate substantially deep into the structure, and, importantly, if the penetration depth would depend on the incidence angle.

The wave reflecting from chirped photonic structures can reflect from the different depth, as shown in Fig. 17 a. This brings to an idea, that chirped mirror could provide negative spatial dispersion, and consequently, can lead to flat focusing mirror.
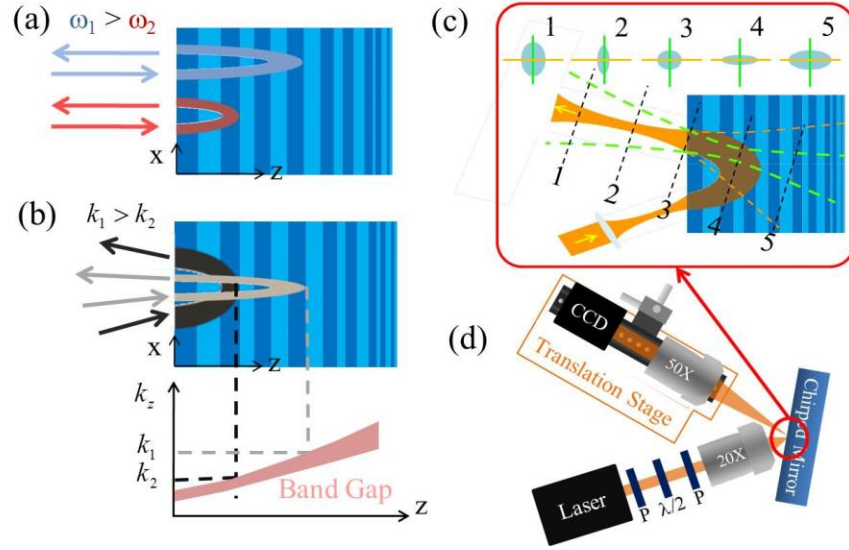
Fig. 17. Principle of a 1D chirped mirror (a), oblique incidence (b). Expected scenario for the focalization of light beams (c). Experimental setup used to observe the cross sections of reflected beam at different positions (d).

If we consider different incidence angle instead of different frequency (Fig. 17 b), plane-wave components will also reflect at different depths. This happen because plane-waves at larger incidence angles have shorter longitudinal component of the wave-vector, so their propagation and reflection is equivalent to that of at normal incidence waves at lower frequency. Since the waves will follow paths with different optical lengths, it will bring about angular-dependent phase delays. These delays can lead to negative spatial dispersion and to beam focusing as illustrated in Fig. 17 c. Here a beam focused in front of the structure undergoes positive spatial dispersion before reflection, negative dispersion inside the structure during reflection, and again positive spatial dispersion propagating in free space after reflection. The free-space positive dispersion balances the negative dispersion in the structure and leads to focusing of the beam at a certain distance from the mirror. The derivative of the phase versus k_x gives the lateral shift of the beam, $s = -d\phi/dk_x$ (also called the Goos-Hanchen shift), whereas the second derivative of the phase versus k_x determines the diffractive broadening of the beam. The latter can be characterized by means of a "diffractive propagation distance" $L_{diffr} = -k d^2\phi/dk^2{}_x$ which gives an equivalent beam propagation distance in vacuum.

We have checked this very rough estimation by numerical calculations considering a concrete 1D chirped structure consisting of 20 periods of two alternating dielectric layers with low (n_1=1.5) and high (n_2=2.17) refractive indices at 532 nm wavelength. A standard transfer matrix method has been used to calculate the reflection coefficient for this structure (Fig. 18). Due to the chirp a broadened angular band-gap is obtained (black line), covering the whole angular range between the unchirped structures bandgaps. Fig. 18 b and c shows the angular dependence of the lateral beam shift s and the diffractive propagation distance L_{diffr} (continuous lines), respectively. Both plots show the expected tendencies according to our analytical estimations, also represented by dashed lines. The estimated tendency, however, is strongly overlaid by a fringe structure. The origin of these fringes lies in the coupling between the forward and backward waves and interference at the surface. This fringing effect can be controlled by modifying the chirp function. However, importantly, at particular angular ranges, the fringes strongly increase the searched effect of negative diffraction. The L_{diffr} becomes thus strongly negative, and the searched effect becomes even larger than analytically estimated.
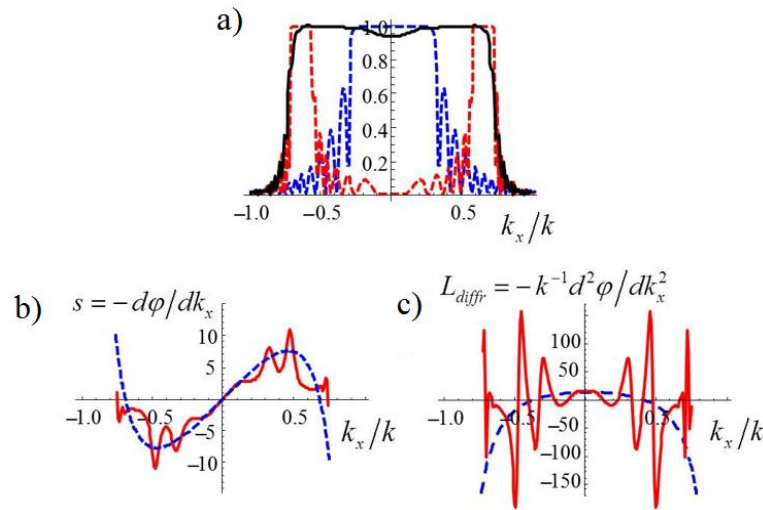

Fig. 18. TE polarization reflectance of chirped structure (continuous black line). The dashed curves correspond to the reflectance of an unchirped structure with the period equal to that of the front (red) and rear (blue) face of the chirped structure. Lateral shift of the light beam (b), spatial dispersion (diffractive propagation) distance (c). In b,c the dashed-line curves correspond to analytical estimations from.

Global pictures of beam reflection were obtained by numerical calculation using the finite difference time domain (FDTD) method in 2D domain. The results for the structure described previously are shown in Fig. 19. A clear focalization is obtained for reflected TE polarized beam. In Fig. 19 b we show three perpendicular cross-sections of the reflected beam, at different positions. The beam profiles for TE polarization clearly show an elliptic shape with the shorter axis within the incidence plane (since the focusing effect appears only in that direction). In contrast, for TM polarization this focusing effect does not appear at this particular incidence angle, and the beam profiles are similar to reflecting from a usual metallic mirror.

In order to prove experimentally the predicted effect, we have built a 1D chirped mirror, and focused a beam of CW laser in front of structure, as schematically shown in Fig. 17 d. All parameters and conditions correspond to those used in FDTD calculations. The reflected beam transverse profile was imaged into a CCD camera. Fig. 19 c shows the recorded images, at the same distances from the mirror surface as in the numerical calculations.
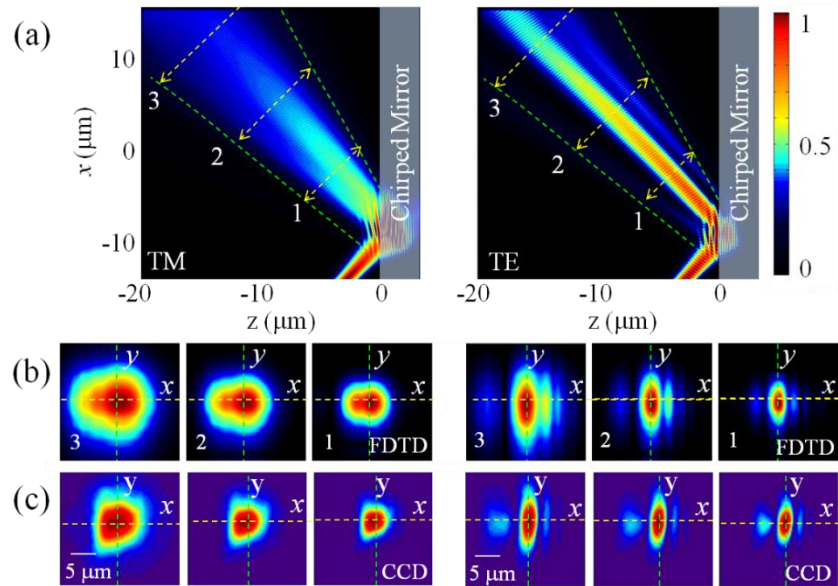

Fig. 19. Beam reflection from 1D chirped structure for TM (left pictures) and TE (right pictures) polarization, at a particular incidence angle of 54º: *a*) beam profile within the plane of incidence; b),c) beam cross sections at the corresponding transverse planes 1, 2 and 3 indicated in a). a),b) show the FDTD calculations, and c) – experimental CCD images. As a reference, the broadening of the same beam reflecting from a metallic mirror is also plotted (green dashed line).

The focusing depends on the incidence angle, with areas of negative L_{diffr} values (focusing) alternating with areas of positive L_{diffr} (defocusing). To check this scenario we fixed an observation plane parallel to the mirror's face (z=-5 µm), and recorded the transverse beam profiles for different incidence angles. Fig. 20 summarizes numerical and experimental results. It shows that the focusing is strongly dependent on the incidence angle, indicating particular ranges where the effect is more pronounced. We focus on two particular angles: 42° and 54° (vertical dashed lines in Fig. 4a). Fig. 4b shows strong focusing for TE polarization at 54° (ellipse compressed in the x direction) and practically no effect for TM polarization. In contrast, at 42° the scenario changes resulting in strong focusing/collimation for TM polarization (with a single dominant elliptic profile) and focusing with fringes (two comparable elliptic profiles close to each other) for TE polarization.
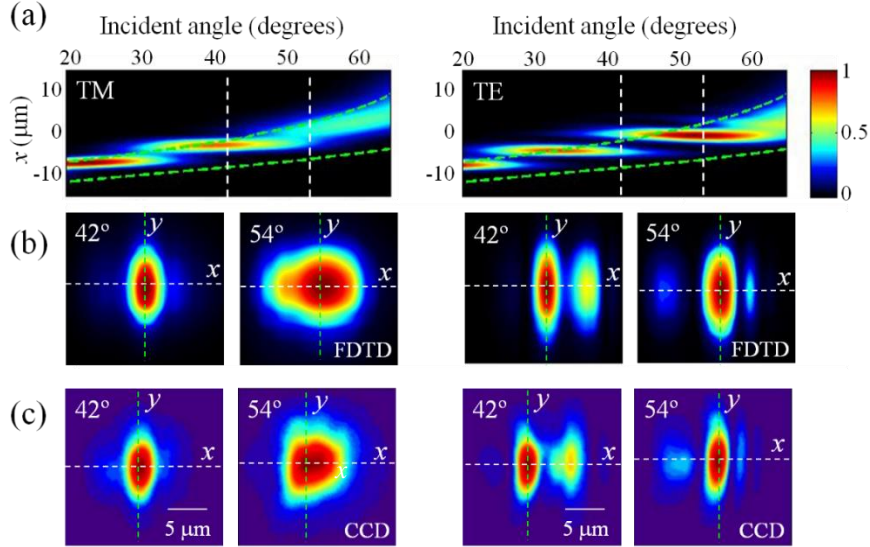

Fig. 20. FDTD simulations of beam reflection from the 1D chirped structure for TM (at the left) and TE (at the right) polarization: a) the vertical cuts at a distance z=-5 µm with different incident angles; b) beam cross sections for two particular incidence angles of 42° and 54° are plotted. These two angles are indicated in a) by vertical dashed lines. The green dashed lines in a represent the position and width (at $1/e^2$ intensity level) of the beam reflected on a metallic mirror; c) experimental CCD images obtained for equivalent conditions.

Chirped mirror with a defect layer

Flat focusing in a chirped mirror was demonstrated earlier. The angular dependence of the phase shift, however, was not monotonic as initially expected. For instance, the slope of lateral shift on the incidence angles is not anomalous for all range of incidence angles, but is separated by areas with the normal slopes. The peaks of negative diffraction appear as the slope changes from positive to negative and they results in the fringes of dispersion curves. These fringes correspond to high values of anomalous diffractions in narrow angular ranges. Several peaks of anomalous diffraction can even enhance the focusing performance. One possibility to enhance the peaks of anomalous diffractions is to introduce a defect into the structure as depicted in Fig. 21 b. For instance, a Gires-Tournois interferometer (GTI) is composed of a defect layer in between of two mirrors: the front mirror partially and the back mirror highly reflective. It could introduce a large, narrow peak of anomalous dispersion in chromatic or angular spectra. The large anomalous dispersion appears in a very narrow spectral (angular) range, therefore a focusing is practically absent for a simple GTI structure. On the other hand, a chirped mirror with a defect layer is proposed in this chapter to provide larger anomalous diffraction in a broader angular bandwidth to give a larger focal length.
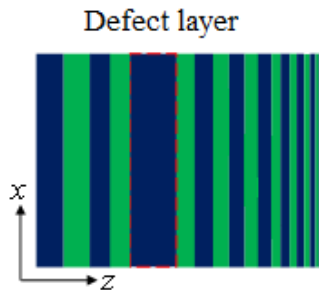

Fig. 21. A defect layer introduced at the fifth layer in the chirped mirror is framed with the red dashed line.

The chirped mirror in our calculations is composed of the layers of alternating high and low refractive index materials with $n_H = 2.17$ and $n_L = 1.49$ for the wavelength 532 nm. The thickness of the defect layer is supposed to be double of the original layer. Fig. 22 a shows the numerical focal length, calculated as the second order derivative of the phase

of refractive coefficient with respect to incidence angles, for different positions of defect from 2-nd to 8-th layer of the chirped mirror structure.
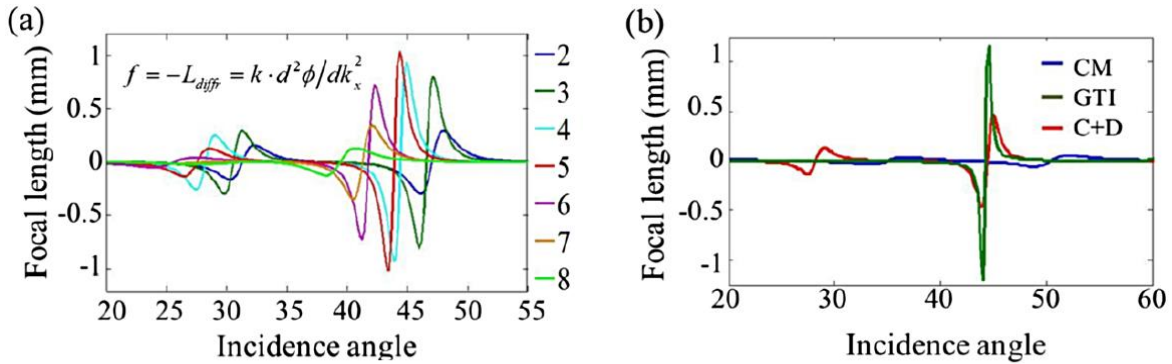

Fig. 22. The focal length depends on different incidence angles for different locations of defect layer from the second to eighth layers (a). The comparison of the focal length between the chirped mirrors (blue), GTI structure (green), and the chirped mirror with a defect located at the fifth layer (red) (b).

The largest numerical focal length was obtained when the defect was positioned on the 5-th layer. Importantly, after introducing a defect layer in the chirped mirror, the angular ranges for positive focal length remain nearly the same but the value of the diffractive length is largely enhanced as shown in Fig. 22 b. It is also noted that the angular variance of this proposed structure is broader than the one of a simple GTI structure (green line) because the layers behind the defect layer act as a chirped mirror reflecting a broad range of angular components.

Fig. 23 shows the field distribution inside the structure depending on the incidence angles. It shows that the smaller incidence angles can penetrate deeper and the lager one reflects in advance. For instance, both the peaks of the focal length and the field enhancement in the defect case appear at incidence angle at 29º and 45º. The stronger focal length at 45º contributes stronger field enhancement.
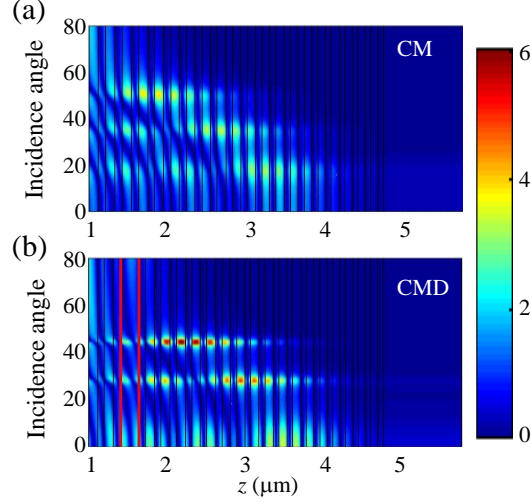
Fig. 23. The 2D map of field inside the mirror structures depending on the incidence angle for (a) the chirped mirror and (b) the chirped mirror with a defect at 5th layer. The interface between air and the structure is at $z = \mu$m. Each black line indicates the boundary of each layer. The position of defect layer is marked in red lines.

The focal length cannot be obtained directly from the formula $F = -L_{diffr} = k \cdot d^2\phi/dk_x^2$ which is used in Fig. 22. It is because that the different plane wave components of the beam located inside the positive peak of the focal length experience different negative diffraction length. The peak value of numerical focal length does not represent the focusing distance from the mirror. Nevertheless, it can indicate the focusing angle at 45° where the slope of lateral shift (the first derivation) on angles is negative or the numerical focal length (the secondary derivation) is positive. It should be also noted that when the incident angle is slightly smaller or larger than the focusing angle, the plane wave components of the beam experience normal and anomalous diffraction simultaneously which results in beam splitting. Fig. 24 shows the focusing performance is calculated by the paraxial model at the incidence angle 45°. The diverging reflected beam from the conventional metallic mirror is shown in Fig. 24 c. The source is positioned at $l_{object} = 5$ µm in front of the mirror and the width of source beam is 8 µm. The wavelength of the source is 532 nm and the TE polarization is considered. The focal distance in reflection can be increased from $l_{image} = 14$ µm to $l_{image} = 34$ µm as expected as the source is fixed at $l_{object} = 5$ µm. The focal length F of near-field focusing $F = l_{image} + l_{object}$ is

34

increased from 19 µm to 39 µm. We note that the focal distance $F = 39$ µm is within the near field area, as the distance is smaller than Rayleigh range of our beam source, $Z_r = W^2/\lambda = 8^2/0.532 = 120$ µm.
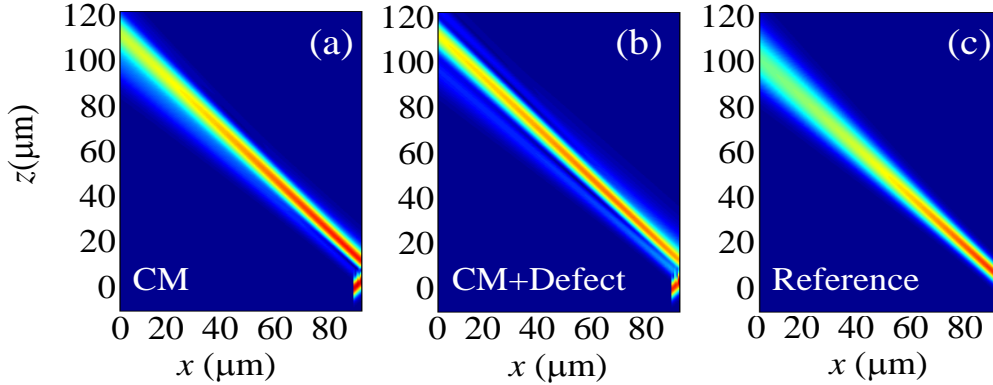

Fig. 24. The beam propagation in reflection for chirped mirror (a), chirped mirror with a defect (b) and the metallic mirror (c) (as a reference beam) at the angle of 45º for TE polarization.

Optimization of chirped mirror structure to enhance focusing performance

In this part, we have adopted a new approach: we have designed and built a particular dielectric mirror structure, which provides the predefined angular delays needed for strong focusing, and then we have demonstrated such focusing by numerical simulations and experiments. A numerical iteration technique was applied to design a multilayer mirror structure with the predefined dispersion by combining a "needle optimization" technique [35] and a gradual evolution approach [51]. The optimization procedure converged to a specific design structure, consisting in our particular case of 98 layers, which provides a segment of linear angular dispersion of around 8 degrees, as depicted in Fig. 25 b. For simplicity, the structure with a defined dispersion was designed for TE polarization only, the dispersion for TM polarization being "uncontrolled" (advanced optimization techniques in principle could allow tailoring dispersions for both polarizations simultaneously). The optimized mirror, as depicted in Fig. 25 a, can be identified as a combination between a chirped mirror structure and a GTI structure (Gires-Tournois Interferometer [52]). Whereas chirped mirrors provide weak dispersion in a broad spectral range, a GTI structure can provide larger dispersion in a narrow spectral range.

Intensity distributions of the reflected beam were calculated using the transfer matrix method. Fig. 25 c shows the focusing effect at the particular incidence angle of 46° corresponding to the middle of the area with negative slope of the angular dispersion curve.
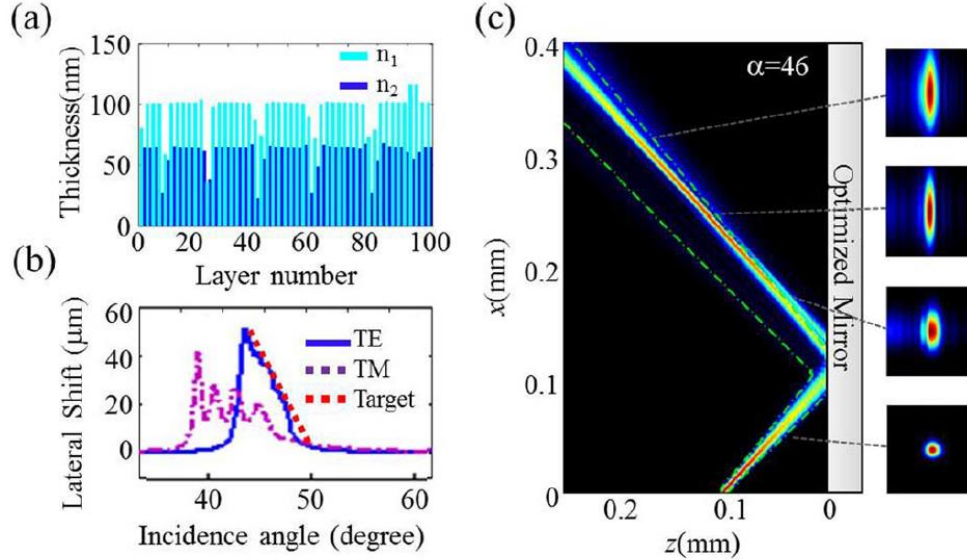

Fig. 25. The mirror with optimized structure. Physical thickness of the layers in the structure consisting of alternating layers of low $n_1 = 1.49$ and high $n_2 = 2.17$ refractive index material (a). Lateral shift of the wave, versus incidence angle (b). The target function is depicted in red dashed line. Beam profile at the optimum angle of 46° for TE polarization, and the resulting 2D cross section of the reflected beam at different propagation distances (c). Green dashed line represents the reflection from a conventional mirror.

The incident beam was focused at a distance of 100 µm in front of the mirror surface with a beam waist diameter of 8 µm. A clear focalization in reflection, with a minimum beam width of 8.5 µm, was obtained with maximum power concentration at 150 µm in front of the mirror along the beam axis direction, for TE polarized beam. This results in a focal distance of 250 µm. Since the focusing effect occurs only within the incidence plane, the beam profiles for TE polarization show elliptic shapes with the shorter axis in the direction of incidence plane, as depicted in Fig. 25 c. Mirror samples for experimental measurements were fabricated using ion beam sputtering technique [53] and Ta_2O_5 and SiO_2 were used as high and low refractive index materials, respectively. To observe the focusing effect in reflection the incident beam at 532 nm, from a CW solid state laser, was focused by at a distance of 40 µm in front of the mirror with a diameter of 8 µm. The reflected beam was recorded by a CCD camera. The position of the x50 imaging objective

and consequently the plane imaged by the CCD camera was precisely controlled with a high resolution (0.5 µm) closed-loop step motor. We observe that the cross-sections of the reflected beam are strongly elongated ellipses. The beam profiles in x direction, for propagation distances ranging from 0 to 240 mm, recorded in steps of 5 mm, are shown in Fig. 26 for both polarizations, showing the strongest focusing at $l_{\text{mage}} = 110$ µm, in the TE case, for a 46°. The focal length is thus estimated to be f = 150 µm. For comparison, the focusing peak is absent for TM polarized beam measurements, which corresponds well to the numerical simulations.
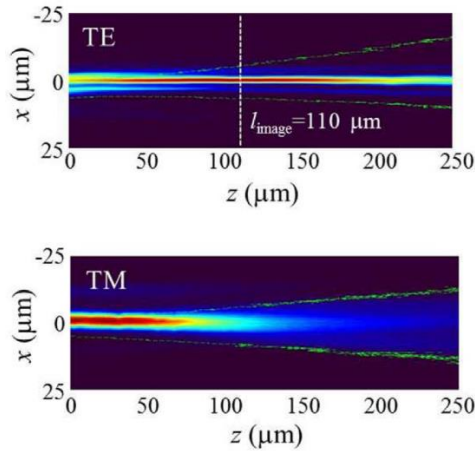
Fig. 26. Beam profiles at the optimum incidence angle of 46° for TE and TM polarization.

The experimentally measured focal length for TE polarized beam, f = 150 mm, is smaller than the numerically estimated one, f = 250 mm, for the same structure. The discrepancy is due to fabrication errors, which for the dielectric mirror of 98 layers is hardly possible to avoid. To be confident on the role of fabrication errors, we performed a numerical simulation introducing a random error in the thickness of the layers. The randomization of the width of the layers by 1.5% (which is the estimated fabrication precision of our samples) results in reduction of the focal distance by around 50–100 mm. The focusing was experimentally obtained in the range of incidence angles from 45 to 47 degrees, in a smaller than that calculated numerically. This difference can be also attributed so the fabrication errors of the thickness of the layers. The maximal focal length is obtained at the incidence angle 46 degrees in a good agreement with our simulation result. The

reported flat focusing mirror contains some apparent limitations: focalization appears only at nonzero incidence angles, and it occurs only in one lateral direction.

In conclusion, we have proposed, and experimentally demonstrated, a new concept of flat focusing mirror without any optical axis. This mirror can focus and reproduce transverse light patterns benefiting, at the same time, from lateral translational invariance. The focusing distances are in the micrometer range, reaching typical distances of 150–250 mm, which make the mirror suitable to build small-scale photonic devices or circuits, in which narrow beams could propagate diffraction free without a waveguide.

Main results and conclusions

1. Spectral shift to longer wavelengths is observed after post-deposition annealing for both monolayer and multilayer Nb_2O_5–SiO_2 coatings. This effect can be explained by changes in the physical and optical properties of materials: the physical layer thickness is increased more than the refractive index, thus leading to an increased overall optical thickness.

2. A surface roughness (RMS) increase was noticed only for layers containing the SiO_2 fraction. For pure SiO_2, RMS increases by up to 10 %. Meanwhile, for Ta_2O_5 and Nb_2O_5 thin films, the roughness change was not observed up to 500 °C of the annealing temperature.

3. In Nb_2O_5–SiO_2 mixtures, the residual stress was found to depend on the peak annealing temperature and the composition of thin films. Changes in stress are attributed to differences in the thermal expansion coefficient between the substrate and the film, as well as to microstructural changes and relaxation.

4. Residual stress in the multilayer is equal to the average stress in materials used for the coating. This was confirmed up to the 500 °C annealing temperature, thus proving that interfaces among different materials have a negligible effect the residual changes.

5. Using mixtures and annealing, a BASIC mirror with an average GVD = –200 fs^2 and 200 nm spectral bandwidth at the center wavelength of 800 nm was made using the ion beam sputtering technology.

6. The LIDT values in mixed oxide layers strongly depend on the bandgap of a layer in both femtosecond and nanosecond regimes. The LIDT values are increased more than the lower refractive index (the wider bandgap) material fraction is increased.

7. Using the HfO_2 and SiO_2 mixtures in combination with annealing can lead to an increase in LIDT values for 355 nm high reflectors in the ns regime up to 3 times (from 4 to 14 J/cm^2). The increase in the LIDT values is explained by the reduction of absorption centers with the annealing procedure and the use of wider band gap mixtures as H layers in a multilayer coating.

8. The laser-induced damage in negative dispersion coatings at the fs regime is caused and limited by the electric field distribution with respect to low band gap materials (Nb_2O_5). The damage morphology inspection has revealed that a damage occurs at the highest electric field position on a high refractive index material.

9. The LIDT values in negative dispersion mirrors were increased by a factor of 2 (from $0.13 \, J/cm^2$ to $0.26 \, J/cm^2$ at 1030 nm and 200 fs pulse length) after reallocating the electric field distribution so that the maximum of the electric field would be on the high band gap SiO_2 material.

10. It has been noted that a beam of a single wavelength can be focused in one dimension, then reflecting from a modulated layer thickness flat chirped mirror at 45 AOI for TE polarization. The focusing effect is created after the negative dispersion in the multilayer is overcompensated by the positive one as the beam after reflection propagates in a free space.

11. It is possible to improve the focal distance from 19 to 39 µm of a flat focusing mirror with a linearly modulated layer thickness by incorporating a resonant layer and thus creating the GTI effect.

12. A focal distance of 110 µm was demonstrated for a flat focusing mirror, for the TE polarization at 46 AOI with the layer structure optimized by multiple GTI structures in one combination. A strong deviation from theoretical values can be explained by the deposition errors in layer thicknesses.

References

[1]   T. H. Maiman, Stimulated Optical Radiation in Ruby, Nature, **187**(4736), 493-494 (1960).

[2]   A. L. Schawlow and C. H. Townes, Infrared and Optical Masers, Physical Review, **112**(6), 1940-1949 (1958).

[3]   E. P. Ippen, C. V. Shank, and A. Dienes, Passive mode locking of the cw dye laser, Applied Physics Letters, **21**(8), 348-350 (1972).

[4]   T. R. Schibli, O. Kuzucu, K. Jung-Won, E. P. Ippen, J. G. Fujimoto, F. X. Kaertner, *et al.*, Toward single-cycle laser systems, IEEE J. Sel. Topics Quantum Electron., **9**(4), 990-1001 (2003).

[5]   R. L. Fork, C. H. Brito Cruz, P. C. Becker, and C. V. Shank, Compression of optical pulses to six femtoseconds by using cubic phase compensation, Opt. Lett., **12**(7), 483-485 (1987).

[6]   E. Treacy, Optical pulse compression with diffraction gratings, IEEE Journal of Quantum Electronics, **5**(9), 454-458 (1969).

[7]   R. L. Fork, O. E. Martinez, and J. P. Gordon, Negative dispersion using pairs of prisms, Opt. Lett., **9**(5), 150-152 (1984).

[8]   J. Heppner and J. Kuhl, Intracavity chirp compensation in a colliding pulse mode-locked laser using thin-film interferometers, Applied Physics Letters, **47**(5), 453-455 (1985).

[9]   R. Szipöcs, K. Ferencz, C. Spielmann, and F. Krausz, Chirped multilayer coatings for broadband dispersion control in femtosecond lasers, Opt. Lett., **19**(3), 201-203 (1994).

[10]   B. Golubovic, R. R. Austin, M. K. Steiner-Shepard, M. K. Reed, S. A. Diddams, D. J. Jones, *et al.*, Double Gires-Tournois interferometer negative-dispersion mirrors for use in tunable mode-locked lasers, Opt. Lett., **25**(4), 275-277 (2000).

[11]   R. Szipöcs, A. Köházi-Kis, S. Lakó, P. Apai, A. P. Kovács, G. DeBell, *et al.*, Negative dispersion mirrors for dispersion control in femtosecond lasers: chirped dielectric mirrors and multi-cavity Gires–Tournois interferometers, Appl. Phys. B, **70**(1), S51-S57 (2000).

[12]   S. Kane and J. Squier, Grism-pair stretcher–compressor system for simultaneous second- and third-order dispersion compensation in chirped-pulse amplification, J. Opt. Soc. Am. B, **14**(3), 661-665 (1997).

[13]   V. Pervak, V. Fedorov, Y. A. Pervak, and M. Trubetskov, Empirical study of the group delay dispersion achievable with multilayer mirrors, Opt. Express, **21**(15), 18311-18316 (2013).

[14]   V. Pervak, C. Teisset, A. Sugita, S. Naumov, F. Krausz, and A. Apolonski, High-dispersive mirrors for femtosecond lasers, Opt. Express, **16**(14), 10220-10233 (2008).

[15]   V. Pervak, A. V. Tikhonravov, M. K. Trubetskov, S. Naumov, F. Krausz, and A. Apolonski, 1.5-octave chirped mirror for pulse compression down to sub-3 fs, Appl. Phys. B, **87**(1), 5-12 (2007).

[16]   V. Pervak, I. Ahmad, M. K. Trubetskov, A. V. Tikhonravov, and F. Krausz, Double-angle multilayer mirrors with smooth dispersion characteristics, Opt. Express, **17**(10), 7943-7951 (2009).

[17]   F. X. Kärtner, N. Matuschek, T. Schibli, U. Keller, H. A. Haus, C. Heine, *et al.*, Design and fabrication of double- chirped mirrors, Opt. Lett., **22**(11), 831-833 (1997).

[18]   N. Matuschek, F. X. Kartner, and U. Keller, Analytical design of double-chirped mirrors with custom-tailored dispersion characteristics, IEEE J. Quantum Electron., **35**(2), 129-137 (1999).

[19]   T. R. Schibli, O. Kuzucu, K. Jung-Won, E. P. Ippen, J. G. Fujimoto, F. X. Kaertner, *et al.*, Toward single-cycle laser systems, IEEE J. Sel. Topics Quantum Electron., **9**(4), 990-1001 (2003).

[20]   G. Steinmeyer, Brewster-angled chirped mirrors for high-fidelity dispersion compensation and bandwidths exceeding one optical octave, Opt. Express, **11**(19), 2385-2396 (2003).

[21] P. Baum, M. Breuer, E. Riedle, and G. Steinmeyer, Brewster-angled chirped mirrors for broadband pulse compression without dispersion oscillations, Opt. Lett.*,* **31**(14), 2220-2222 (2006).

[22] V. Laude and P. Tournois, Chirped-mirror pairs for ultra-broadband dispersion control, in *Lasers and Electro-Optics, 1999. CLEO '99. Summaries of Papers Presented at the Conference on*, 1999, pp. 187-188.

[23] F. X. Kärtner, U. Morgner, R. Ell, T. Schibli, J. G. Fujimoto, E. P. Ippen*, et al.*, Ultrabroadband double-chirped mirror pairs for generation of octave spectra, J. Opt. Soc. Am. B*,* **18**(6), 882-885 (2001).

[24] N. U. Wetter, E. P. Maldonado, and N. D. Vieira Jr, Calculations for broadband intracavity chirp compensation with thin-film Gires-Tournois interferometers, Revista de F sica Aplicada e Instrumenta cão*,* **13**(2), 31 (1998).

[25] N. Matuschek, L. Gallmann, D. H. Sutter, G. Steinmeyer, and U. Keller, Back-side-coated chirped mirrors with ultra-smooth broadband dispersion characteristics, Appl. Phys. B*,* **71**(4), 509-522 (2000).

[26] T. Eidam, S. Hanf, E. Seise, T. V. Andersen, T. Gabler, C. Wirth*, et al.*, Femtosecond fiber CPA system emitting 830 W average output power, Opt. Lett.*,* **35**(2), 94-96 (2010).

[27] O. Pronin, J. Brons, C. Grasse, V. Pervak, G. Boehm, M. C. Amann*, et al.*, High-power 200 fs Kerr-lens mode-locked Yb:YAG thin-disk oscillator, Opt. Lett.*,* **36**(24), 4746-4748 (2011).

[28] M. Lappschies, M. Jupé, and D. Ristau, Extension of Ion Beam Sputtered Oxide Mixtures into the UV Spectral Range, in *Optical Interference Coatings*, Tucson, Arizona, 2007, p. TuA7.

[29] A. Melninkaitis, T. Tolenis, L. Mažulė, J. Mirauskas, V. Sirutkaitis, B. Mangote*, et al.*, Characterization of zirconia– and niobia–silica mixture coatings produced by ion-beam sputtering, Appl. Opt.*,* **50**(9), C188-C196 (2011).

[30] J. T. Brown, Center wavelength shift dependence on substrate coefficient of thermal expansion for optical thin-film interference filters deposited by ion-beam sputtering, Appl. Opt.*,* **43**(23), 4506-4511 (2004).

[31] E. Çetinörgü-Goldenberg, J. E. Klemberg-Sapieha, and L. Martinu, Effect of postdeposition annealing on the structure, composition, and the mechanical and optical characteristics of niobium and tantalum oxide films, Appl. Opt.*,* **51**(27), 6498-6507 (2012).

[32] M. J. Weber, *Handbook of Optical Materials* (Taylor & Francis, 2002).

[33] B. J. Pond, J. I. DeBar, C. K. Carniglia, and T. Raj, Stress reduction in ion beam sputtered mixed oxide films, Appl. Opt.*,* **28**(14), 2800-2805 (1989).

[34] A. E. Ennos, Stresses Developed in Optical Film Coatings, Appl. Opt.*,* **5**(1), 51-61 (1966).

[35] A. V. Tikhonravov, M. K. Trubetskov, and G. W. DeBell, Optical coating design approaches based on the needle optimization technique, Appl. Opt.*,* **46**(5), 704-710 (2007).

[36] A. V. Tikhonravov, M. K. Trubetskov, and T. V. Amotchkina, Investigation of the effect of accumulation of thickness errors in optical coating production by broadband optical monitoring, Appl. Opt.*,* **45**(27), 7026-7034 (2006).

[37] R. Ell, U. Morgner, F. X. KÃÂrtner, J. G. Fujimoto, E. P. Ippen, V. Scheuer*, et al.*, Generation of 5-fs pulses and octave-spanning spectra directly from a Ti:sapphire laser, Opt. Lett.*,* **26**(6), 373-375 (2001).

[38] N. Matuschek, *Theory and Design of Double-chirped Mirrors* (Hartung-Gorre, 1999)

[39]   V. Pervak, O. Razskazovskaya, B. Angelov Ivan, L. Vodopyanov Konstantin, and M. Trubetskov, "Dispersive mirror technology for ultrafast lasers in the range 220–4500 nm," in *Advanced Optical Technologies* vol. 3, ed, 2014, p. 55.

[40]   E. Fedulova, K. Fritsch, J. Brons, O. Pronin, T. Amotchkina, M. Trubetskov, *et al.*, Highly-dispersive mirrors reach new levels of dispersion, Opt. Express, **23**(11), 13788-13793 (2015).

[41]   L. Smalakys, G. Batavičiūtė, E. Pupka, and A. Melninkaitis, Parametric analysis of damage probability: a tool to identify weak layers within multilayer coatings, Appl. Opt., **54**(10), 2953-2962 (2015).

[42]   B. Mangote, L. Gallais, M. Commandré, M. Mende, L. Jensen, H. Ehlers, *et al.*, Femtosecond laser damage resistance of oxide and mixture oxide optical coatings, Opt. Lett., **37**(9), 1478-1480 (2012).

[43]   I. B. Angelov, M. von Pechmann, M. K. Trubetskov, F. Krausz, and V. Pervak, Optical breakdown of multilayer thin-films induced by ultrashort pulses at MHz repetition rates, Opt. Express, **21**(25), 31453-31461 (2013).

[44]   J. Jasapara, A. V. V. Nampoothiri, W. Rudolph, D. Ristau, and K. Starke, Femtosecond laser pulse induced breakdown in dielectric thin films, Physical Review B, **63**(4), 045117 (2001).

[45]   S. John, Strong localization of photons in certain disordered dielectric superlattices, Physical Review Letters, **58**(23), 2486-2489 (1987).

[46]   E. Yablonovitch, Inhibited Spontaneous Emission in Solid-State Physics and Electronics, Physical Review Letters, **58**(20), 2059-2062 (1987).

[47]   C. Luo, S. G. Johnson, J. D. Joannopoulos, and J. B. Pendry, All-angle negative refraction without negative effective index, Physical Review B, **65**(20), 201104 (2002).

[48]   E. Cubukcu, K. Aydin, E. Ozbay, S. Foteinopoulou, and C. M. Soukoulis, Electromagnetic waves: Negative refraction by photonic crystals, Nature, **423**(6940), 604-605 (2003).

[49]   Z. Lu, J. A. Murakowski, C. A. Schuetz, S. Shi, G. J. Schneider, and D. W. Prather, Three-Dimensional Subwavelength Imaging by a Photonic-Crystal Flat Lens Using Negative Refraction at Microwave Frequencies, Physical Review Letters, **95**(15), 153901 (2005).

[50]   G. V. Viktor, The electrodynamics of substances with simultaneously negative values of and μ, Soviet Physics Uspekhi, **10**(4), 509 (1968).

[51]   A. V. Tikhonravov, M. K. Trubetskov, T. V. Amotchkina, and M. A. Kokarev, Key role of the coating total optical thickness in solving design problems, 2004, pp. 312-321.

[52]   C. A. Rivera, S. E. Bradforth, and G. Tempea, Gires-Tournois interferometer type negative dispersion mirrors for deep ultraviolet pulse compression, Opt. Express, **18**(18), 18615-18624 (2010).

[53]   S. Chao, W.-H. Wang, and C.-C. Lee, Low-loss dielectric mirror with ion-beam-sputtered TiO2–SiO2 mixed films, Appl. Opt., **40**(13), 2177-2182 (2001).